Depolarization of diffusely reflecting man-made objects

Brian J. DeBoo, Jose M. Sasian, and Russell A. Chipman

The polarization properties of light scattered or diffusely reflected from seven different man-made samples are studied. For each diffusely reflecting sample an in-plane Mueller matrix bidirectional reflectance distribution function is measured at a fixed bistatic angle using a Mueller matrix imaging polarimeter. The measured profile of depolarization index with changing scattering geometry for most samples is well approximated by an inverted Gaussian function. Depolarization is minimum for specular reflection and increases asymptotically in a Gaussian fashion as the angles of incidence and scatter increase. Parameters of the Gaussian profiles fitted to the depolarization data are used to compare samples. The dependence of depolarization on the incident polarization state is compared for each Stokes basis vector: horizontal, vertical, 45°, 135°, and right- and left-circular polarized light. Linear states exhibit similar depolarization profiles that typically differ in value by less than 0.06 (where 1.0 indicates complete depolarization). Circular polarization states are depolarized more than linear states for all samples tested, with the output degree of polarization reduced from that of linear states by as much as 0.15. The depolarization difference between linear and circular states varies significantly between samples.   © 2005 Optical Society of America

OCIS codes: 120.5410, 120.5820, 230.5440, 290.5880.

1. Introduction

Polarimetry of scattered light, or scatter polarimetry, measures the relationship between incident polarized light and the polarization of diffusely and specularly reflected light from a scattering object or surface. Scatter polarimetry characterizes the light-scattering phenomenology of actively illuminated objects. Compared with intensity images, the measured polarization properties provide additional information to characterize actively illuminated surfaces. A polarimetry technique that measures all polarization coupling properties, usually in the form of Mueller matrices, can characterize the light-scattering process in terms of the standard polarization element properties: diattenuation, retardance, and depolarization. Whereas typical optical elements (e.g., lenses or prisms) have little depolarization, most natural and man-made objects exhibit significant depolarization. Depolarization dominates the polarization prop-

erties for all the samples examined in this study, which exhibit negligible retardance and only small amounts of diattenuation.

Early studies of polarization in scattered light were performed by Mie,[1] Beckman and Spizzichino,[2] and are summarized by Stover.[3] Large numbers of theoretical and experimental scatter polarization studies have been conducted, including the work presented in Refs. 4–17. A few studies have modeled depolarization during the light-scattering interaction.[13,14] Scatter polarization measurements (often including depolarization) have been published for several surfaces, including a one-dimensional rough steel surface by Nee and Nee,[6] roughened aluminum by Lewis *et al.*,[16] satellite materials including Tedlar and Teflon-coated aluminum by Sornsin and Chipman,[5] and rough gold and glass surfaces by Hoover *et al.*[17] Depolarization has been measured using ellipsometry.[6] Pezzaniti and Chipman measured a Mueller matrix bidirectional reflectance distribution function (MmBRDF) for a diamond-turned mirror using a Mueller matrix imaging polarimeter (MMIP) technique similar to the method used in this work.[4]

A primary motivation for research in scatter polarimetry is to gain understanding of the interaction of polarized beams with natural scenes and to search for useful discriminants to classify objects at a distance.

This work surveys the scatter polarization properties of seven different man-made samples (e.g., fabric, concrete, metal) by comparing polarization signa-

When this research was performed, the authors were with the Optical Sciences Center, University of Arizona, 1630 East University Boulevard, Tucson, Arizona 85721. B. J. DeBoo (brian.deboo@goodrich.com) is currently with the Goodrich Corporation, 100 Wooster Heights, Danbury, Connecticut 06810.

tures measured with a MMIP. This study differs from previous research in its evaluation of the depolarization index of samples and the evaluation of how depolarization varies with different incident polarization states.

Mueller matrix imaging polarimetry and light-scattering measurement techniques are combined by measuring Mueller matrix images for scattered and diffusely reflected light across a range of incident and scattering angles. This combination of Mueller matrices and scattering is formulated in terms of the MmBRDF. The MmBRDF is measured for each sample in a single plane of incidence and scatter. In this way, the Mueller matrix data as well as the reduced polarimetric data (e.g., depolarization and diattenuation) are studied as a function of scattering geometry.

Since scatterers are often good depolarizers, depolarization is a valuable metric (with a large range) used to characterize scattering materials. The variation of depolarization with scattering geometry for a majority of the man-made samples measured exhibits a functional form well fit by inverted Gaussian functions (although other profiles have been observed elsewhere).[18,19] The shape of the depolarization profile and corresponding fit depends on surface roughness and reflectivity. The mathematical parameters defining the Gaussian shapes fitted to depolarization data are under investigation for classifying surfaces and estimating surface roughness.

Appendix A contains material describing Mueller matrices and their decomposition, the difference between transmission coordinate systems and the reflection coordinate system for scattering, and depolarization metrics. The magnitude of depolarization is quantified by the depolarization index, $\text{Dep}(\mathbf{M})$,

$$\text{Dep}(\mathbf{M}) = 1 - \frac{\sqrt{\left(\sum_{i,j} m_{ij}^{2}\right) - m_{11}^{2}}}{\sqrt{3}\, m_{11}}, \qquad (1)$$

where the m_{ij} are Mueller matrix elements. For nondepolarizing Mueller matrices, $\text{Dep}(\mathbf{M}) = 0$, whereas the ideal depolarizing matrix has $\text{Dep}(\mathbf{M}) = 1$. Scatter measurement geometry and the nomenclature of the MmBRDF are defined in Appendix B. Section 2 presents the experimental configuration and MMIP measurement geometry. The light-scattering MmBRDF measurements for seven man-made samples are presented in Section 3, and the depolarization indices of these samples are discussed in Section 4.

By analyzing the MmBRDF, depolarization as a function of scatter geometry is calculable for arbitrary incident polarizations since Mueller matrices offer complete polarization coupling and decoupling information. Differences in these depolarization profiles with changing incident polarization states are examined in Section 5, where the degree of polarization (DOP) of scattered light is plotted for each input Stokes basis vector. Depolarization of circular polar-

ization states is found to be consistently greater than depolarization for linear input polarizations, but the difference in depolarization between circular and linear states as a function of scatter angle varies substantially from sample to sample.

2. Mueller Matrix Imaging Polarimeter Experimental Configuration

A dual-rotating-retarder MMIP[20] constructed at the Optical Sciences Center was used in the configuration of Fig. 1 to measure the Mueller matrices of seven man-made samples in multiple geometries. Polarimetric data are acquired and reduced into Mueller matrices by the method of Ref. 20. The polarimeter consists of a polarization generator that illuminates the sample with a series of calibrated polarization states and a polarization analyzer that collects the scattered light and analyzes the polarization state. The polarization generator contains an 808 nm laser diode (Hamamatsu L-8446) operating at up to 1 W output power, followed by beam-shaping optics, a fixed linear polarizer, and a rotating linear retarder. The beam illuminating the sample is nearly collimated (less than 3° half-cone angle). The polarization analyzer consists of a rotating retarder and a fixed polarizer followed by imaging optics and a CCD camera. The sample is imaged onto the camera. The collection aperture of the camera subtends a full angle of approximately 3° with respect to the sample. A series of images are acquired as the two retarders are rotated through a series of angles, and the Mueller matrix is calculated on a pixel-by-pixel basis, yielding a Mueller matrix image such as Fig. 13 in Appendix A.

The polarization generator and analyzer subtend a fixed bistatic angle, $\beta = \theta_i + \theta_s$, of 14° with respect to the sample. Both the generator and the analyzer axes and the sample normal are in the same plane (i.e., $\phi_i = 0 = \phi_s$ in the geometric nomenclature of Fig. 14 in Appendix B). Smaller bistatic angles are useful to support remote sensing studies given that many systems measure at long ranges with adjacent generators and analyzers. The physical widths of the
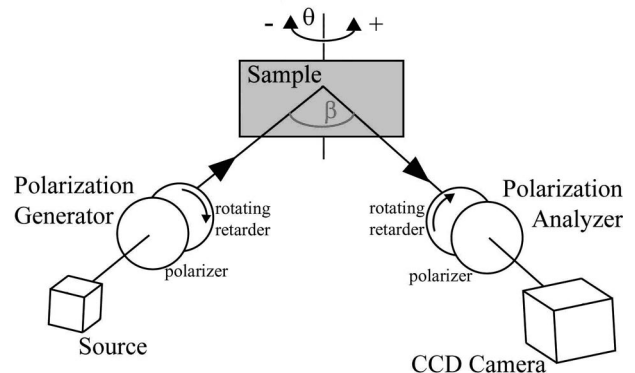

Fig. 1. MMIP used for in-plane MmBRDF measurements, with bistatic angle $\beta = 14°$ between the polarization generator arm and the analyzer arm. The sample rotation angle θ is measured with respect to the specular reflection condition.

generator and analyzer used here prevented bistatic angles smaller than 14°.

Mueller matrix measurements at multiple angles used to construct the MmBRDF are collected by rotating the sample with respect to the fixed polarization generator and analyzer. Each sample is held in a rotary mount and rotated about the axis orthogonal to the plane of incidence (i.e., the y axis of Fig. 14) in 10° steps from $-70°$ to $70°$, where 0° denotes the specular reflection orientation. At each angle, in-plane scattered light is collected and a Mueller matrix is calculated, yielding MmBRDF$(0°, \theta_i, 0°, \theta_i + \beta)$ with a single degree of freedom. For this study, the MmBRDF is measured only in a single plane. Given the 14° bistatic angle, data measured in the 0° sample orientation (i.e., for specular reflection, where the sample normal bisects the MMIP bistatic angle) represent MmBRDF$(0°, -7°, 0°, 7°)$. Measurements for sample rotation angles of $+10°$ and $+20°$ represent MmBRDF$(0°, -17°, 0°, -3°)$ and MmBRDF$(0°, -27°, 0°, -13°)$, respectively, and so forth.

These Mueller matrix images with nearly collimated illumination show significant pixel-to-pixel noise variation due to the roughness of the samples and some spatial nonuniformities. To reduce the effects of measurement noise, the data within each of the 16 component images (e.g., of Fig. 13) are averaged across all pixels, yielding an image-averaged Mueller matrix. Pixels below an intensity threshold are masked off during analysis.

3. Scatter Polarimetry Measurements

Table 1 lists the seven man-made samples measured in this study. Figures 2 through 8 contain the in-plane MmBRDF plots constructed from the normalized, image-averaged Mueller matrix measurements at each of the 15 sample rotation angles. Note that the scale on the diagonal elements is greater than on the remaining Mueller components.

First, the patterns shared by most of the data sets are discussed along with the interpretation of particular matrix elements. Then the retardance properties are shown to be very small for all the samples. Finally, the MmBRDF is discussed in detail for several

Table 1. Man-Made Samples Characterized by Scatter Polarimetry with a MMIP

| Sample	Description
Metal box part	Smooth metal painted dark green
Nylon plastic material	Dark green color, lightweight material
Canvas with paint splotches	Varies in color and material, underlying cloth is greenish-khaki
Sidewalk concrete	Flat, rough surface
Glass diffuser	Frosted on only one side
Gold-coated glass diffuser	Similar to glass diffuser, roughened surface has thin coating of gold
Screen mesh	Finely meshed material, as used for a window screen
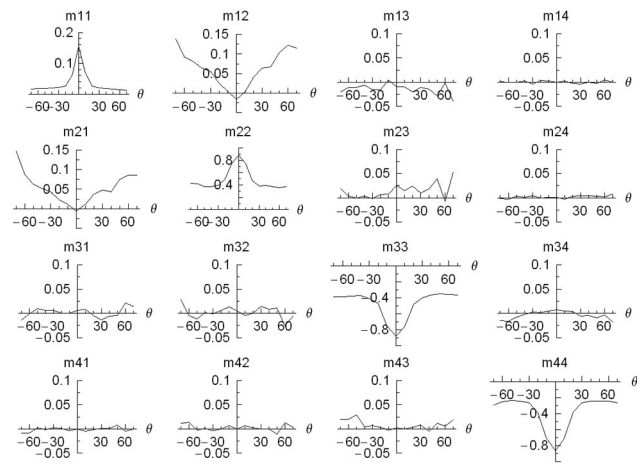
Fig. 2. Normalized in-plane MmBRDF plot for a green painted metal sample. Each of the 4×4 arrays of graphs contains a different Mueller matrix element for the light-scattering process as the sample rotates from $-70°$ to $70°$ with respect to the specular condition (0°).

samples. The depolarization is treated in Sections 4 and 5.

A. Nonzero Elements

The m_{11} element curves contain the variations in scattering of unpolarized light as a function of sample rotation. Samples with large m_{11} peaks at the origin have large specular components, such as the green painted metal and the gold-coated diffuser. Diffusely scattering samples with small specular components have nearly flat m_{11} curves, such as the nylon plastic, screen mesh fabric, and concrete. The glass diffuser is intermediate in this regard, having a small specular peak.

Polarization properties are readily observed directly from the MmBRDF plots, because each of the components of diattenuation and retardance relate to specific Mueller matrix elements. These measured values may be compared against the known and tabulated Mueller matrix forms for different properties,
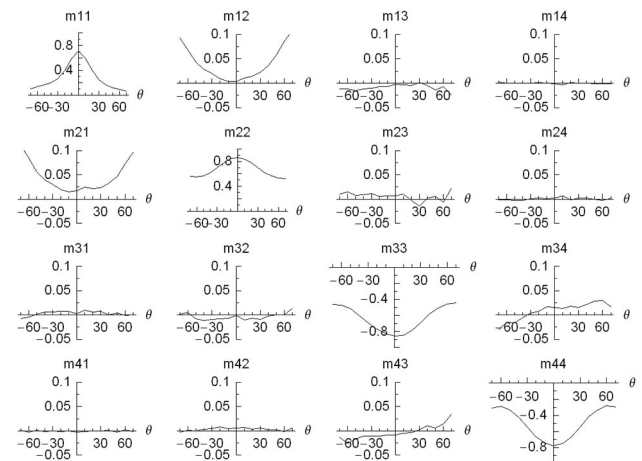

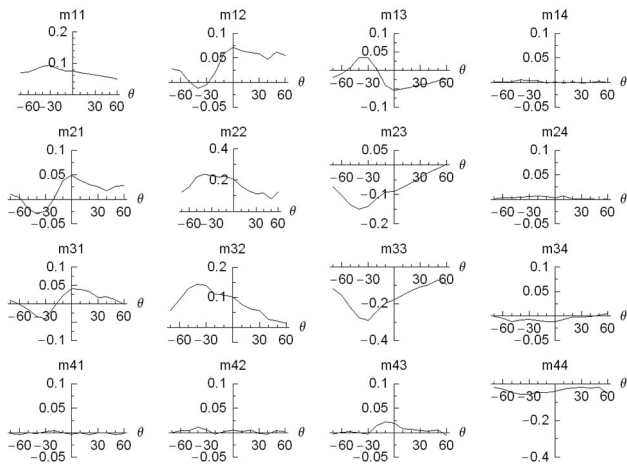Fig. 3. Normalized in-plane MmBRDF plot for gold-coated diffuser as a function of sample rotation angle θ.

Fig. 4. Normalized in-plane MmBRDF plot for screen mesh fabric as a function of sample rotation angle θ.

Fig. 6. Normalized in-plane MmBRDF plot for canvas material as a function of sample rotation angle θ.

remembering to account for the sign convention of reflection measurements and the effect of depolarization on the matrix forms.

The majority of the nonzero values are found in elements m_{11}, m_{12}, m_{21}, m_{22}, m_{23}, m_{32}, m_{33}, and m_{44}. The m_{12} element indicates diattenuation in the s or p plane (for $m_{12} > 0$ or $m_{12} < 0$, respectively). The m_{21} element is closely related in function to m_{12}; nonzero values indicate that s- or p-polarized light is preferentially transmitted, the property of polarizance.

The m_{23} and m_{32} elements are only significantly nonzero for the screen mesh sample, indicative of a coupling between horizontal and vertical polarization and 45° and 135° polarization, due to the structure of its mesh lines.

The other nonzero elements are found along the matrix diagonal. The m_{22} element can be reduced from 1, and m_{33} and m_{44} can be increased from -1 by diattenuation or retardance. This change is a second-order effect arising from the cosine dependence of the
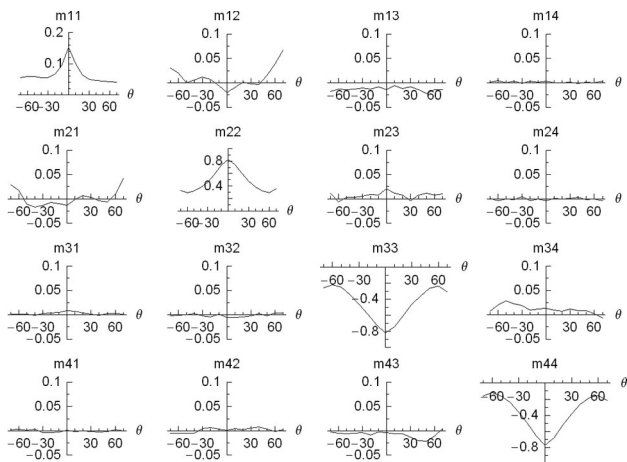
diagonal elements on the magnitudes of diattenuation and retardance. Here the diattenuation and retardance are too small for these second-order terms to introduce significant deviations from 1 and -1. Thus the deviations of m_{22} from 1 and of m_{33} and m_{44} from -1 are predominantly due to depolarization.

B. Near-Zero Elements

Most of the data for elements m_{13}, m_{14}, m_{24}, m_{31}, m_{34}, m_{41}, m_{42}, and m_{43} are very small, within 0.03 of zero. The m_{13} elements indicate little 45° or 135° diattenuation from these samples, and m_{14} indicates little circular diattenuation, as expected. Likewise, small values for m_{31} and m_{41} indicate little polarizance for these 45°, 135°, and circular components.

The uniformly small m_{34} and m_{43} values indicate that these scatterers exhibit very little retardance between the s and p planes. The rough surfaces and scattering process effectively remove whatever retardance that smooth surfaces of these materials would display. The small m_{24} and m_{42} values indicate little retardance at 45° to the s and p planes.

Fig. 5. Normalized in-plane MmBRDF plot for a glass diffuser as a function of sample rotation angle θ. The spike at θ = 0 in the m_{11} element indicates the increase in specular reflection relative to the diffusely scattering background.
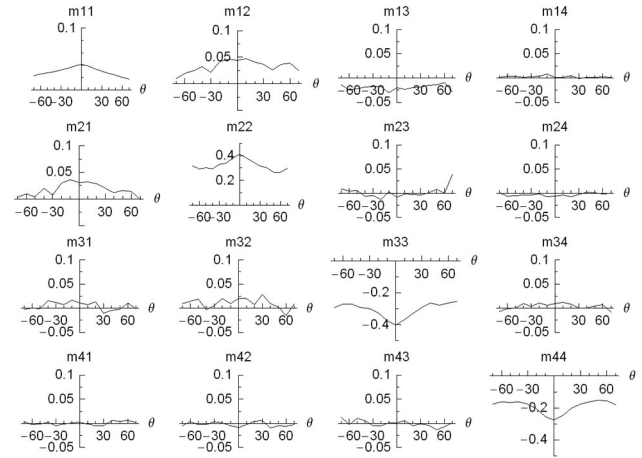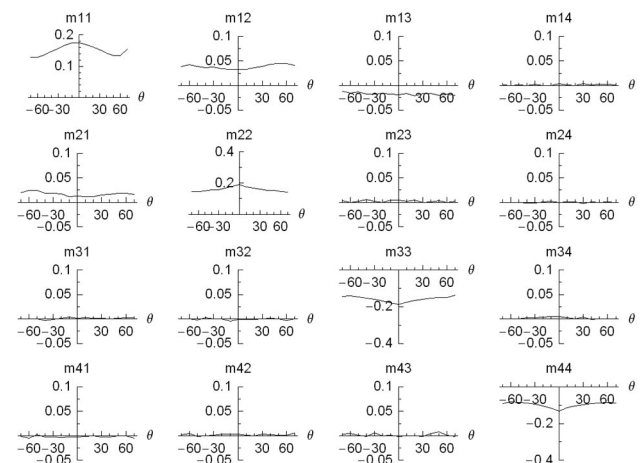

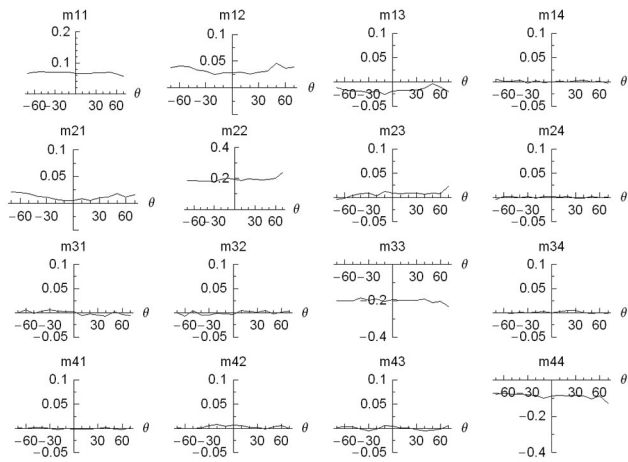Fig. 7. Normalized in-plane MmBRDF plot for concrete as a function of sample rotation angle θ.

Fig. 8. Normalized in-plane MmBRDF plot for green nylon (plastic) material as a function of sample rotation angle θ.

In summary, these samples have negligible retardance and a small diattenuation and polarizance oriented with the s or p planes, but all exhibit significant depolarization. This generalizes some of the ways in which many of the Mueller matrix elements can be interpreted. The following subsections discuss the polarization characteristics of some specific samples.

C. Green Painted Metal

For the green painted metal shown in Fig. 2, m_{11} peaks at 0° (the specular reflection condition) and then rapidly drops for higher angles, a characteristic typical of BRDF curves for relatively smooth surfaces. The elements m_{22}, m_{33}, and m_{44} all have an absolute value of approximately 0.84, making the painted metal sample a nearly uniform depolarizer at 0°. A map of the output DOP shows less than 1% variation in output DOP over all incident polarization states in this measurement geometry. At larger sample angles (see, e.g., Mueller components for a 50° sample rotation angle), the painted metal behaves as a nonuniform depolarizer. At this and other sample rotation angles away from specular, circular states experience greater depolarization than linear states, readily observed by the divergence of the m_{44} component's magnitude from the m_{22} and m_{33} magnitudes as the sample rotation angle increases. As the incident beam moves away from the specular condition, the DOP of scattered light decreases for all polarization states; the painted metal becomes more depolarizing.

The green metal m_{12} and m_{21} curves increase from near zero at the specular condition for sample rotations in both directions. The positive m_{12} element indicates horizontal diattenuation (i.e., p-oriented light diffusely reflects more than s-oriented light), whereas m_{21} indicates horizontal polarizance of approximately the same magnitude. The green painted metal thus behaves as a conventional partial polarizer in diffuse reflection, a condition indicated by equality of diattenuation and polarizance.

D. Gold-Coated Diffuser

Figure 3 is the in-plane MmBRDF for a gold-coated diffuser, a piece of ground glass with vacuum-deposited gold. The patterns in the Mueller matrix elements resemble those for the painted green metal (i.e., the sample behaves as a nearly uniform depolarizer in the specular orientation and a nonuniform depolarizer at larger incidence angles). However, the MmBRDF element curves are broader, as expected from a more reflective sample where more light returns to the detector further from specular reflection. Each of the diagonal elements in the MmBRDF of the gold-coated diffuser shows close agreement with data for a rough gold surface produced by the same processes and measured by Hoover et al.[17] The diattenuation pattern in the m_{12} and m_{21} elements agrees in magnitude with Hoover et al., but differs in sign.

The gold-coated diffuser and green painted metal have the largest diattenuation.

E. Screen Mesh Fabric

The screen fabric has a typical mesh weave with parallel threads woven in two orthogonal directions. During this measurement the threads were rotated 25° from horizontal and vertical. The MmBRDF plot for the screen fabric in Fig. 4 exhibits asymmetric element curves, unlike all the other samples, with most of these Mueller matrix element curves peaking near −40° of sample rotation. Additionally, the m_{12} and m_{13} elements indicate diattenuation that is rotated from horizontal by approximately 25°, the rotation angle of the thread axes about the sample normal. The m_{13} and m_{31} elements are antisymmetric due to the sign change that happens on reflection for 45° and 135° light [see Eq. (A5)].

F. Concrete and Canvas

The concrete is a relatively Lambertian sample; the m_{11} element is nearly flat with a very small specular peak at the origin. The m_{12} element indicates very slight horizontal diattenuation and the m_{21} element indicates only half as much polarizance. At these low levels the concrete is twice as strong of a polarization analyzer as it is a polarizer in output. Horizontal polarized light scatters slightly more efficiently than vertical polarized light, but the output is nearly unpolarized in either case.

The canvas is similar to concrete in the magnitude of its diattenuation and depolarization. The canvas has a larger specular reflection component.

4. Depolarization Profiles

These man-made samples all exhibit significant depolarization in their specular reflected light and more depolarization in the diffusely scattered light. The variation of the depolarization index with sample rotation angle is plotted for five samples in Fig. 9.

The depolarization profiles with changing sample rotation angle resemble inverted Gaussian curves. The minimum depolarization occurs near the specular condition (i.e., sample rotation $\theta = 0°$). Each de-
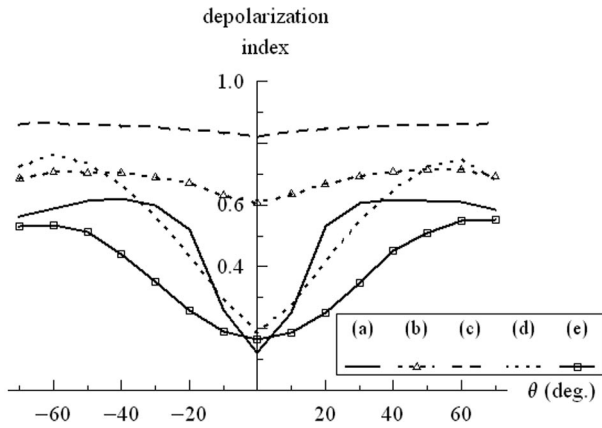
Fig. 9. Depolarization index versus sample rotation angle θ for five man-made scattering samples tends to follow an inverted Gaussian functional form. Labeled plot styles represent (a) painted metal, (b) canvas, (c) concrete, (d) glass diffuser, and (e) gold-coated diffuser. The depolarization index indicates the DOP of the exiting light averaged over all possible polarized incident states. A value of zero indicates no depolarization, whereas a value of one indicates that the scattered light is completely unpolarized for polarized illumination.

Fig. 10. Average depolarization index versus sample rotation angle for the glass diffuser, with inverted Gaussian fit.

polarization profile of Fig. 9 is fit to a Gaussian curve of the form

$$f(x) = K - A \exp(-\theta^2/\sigma^2), \qquad (2)$$

where K is the Gaussian asymptote, A is the Gaussian amplitude, and σ is the $1/e$ half-width of the curve. This inverted Gaussian function was fitted to each of the depolarization index curves of Fig. 9 across the entire range of sample rotation angles ($-70°$ to $70°$). For example, Fig. 10 shows the average depolarization index versus the sample rotation angle for the glass diffuser and the corresponding Gaussian fit.

Table 2 shows the parameters of the Gaussian curves that were fitted to the depolarization profiles of Fig. 9. Accurate fits were obtained with less than an 8.2% rms fitting error in all cases and less than a 3.5% error in three cases, illustrating the applicability of the inverted Gaussian function as a compact expression of depolarization in this configuration. The asymptote parameter K indicates the average DOP of light scattered at large sample rotation angles. The difference between K and A (the Gaussian amplitude) is the average DOP for the specularly reflected beam with a 7° angle of incidence (i.e., half the bistatic angle).
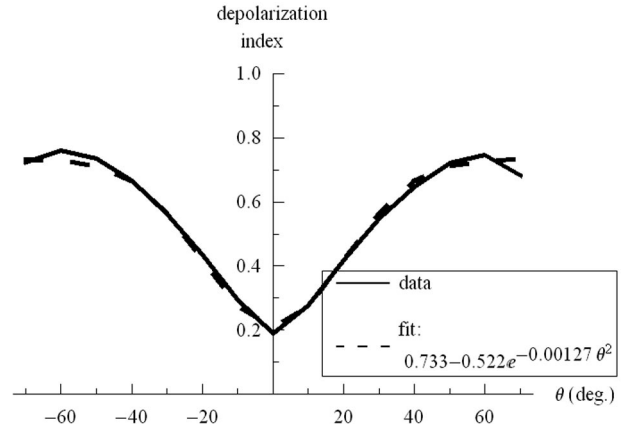
The most reflective sample, the gold-coated diffuser, exhibits the widest depolarization profile. The depolarization asymptote K for the gold-coated diffuser indicates the lowest depolarization level for higher sample rotation angles. Less reflective samples such as the concrete have higher asymptotes.

The green painted metal has the narrowest Gaussian fit to its depolarization profile. The higher reflectivity at the specular condition is related to the lower depolarization since single reflections tend to maintain polarization. The canvas and concrete samples have wide and shallow depolarization signatures with greater asymptote values for large sample rotation angles, indicative of greater roughness and multiple scattering. The concrete sample, having the shallowest profile (smallest A) and the largest asymptote K, is the best depolarizer of the five samples in Fig. 9.

The relative values of the depolarization index at large angles, well described by the asymptote value K of their fitted Gaussian curves, show similar ordering to reflectivity. Roughness does not seem to correlate well to K, nor to amplitude or width. However, the Gaussian slope, or steepness, defined as the ratio of the curve's amplitude to the half-width, does correlate to roughness. The rougher samples like the canvas and concrete exhibit shallow and wide Gaussian depolarization fits with small A/σ. Slightly less rough samples like the diffusers have fitted curves with intermediate values of the Gaussian steepness. The painted metal, the smoothest of the five samples, has the steepest depolarization profile.

Table 2. Shape and Quality Parameters of Gaussian Profiles Fitted to the Average Depolarization Data

Sample	Asymptote (K)	Amplitude (A)	$1/e$ Half-Width (σ)	A/σ	Maximum rms Fit Error (%)
Green painted metal	0.6048	0.5018	15.46	0.0325	6.91
Canvas	0.7029	0.0943	19.99	0.0047	2.76
Concrete	0.8607	0.0330	26.61	0.0012	1.10
Glass diffuser	0.7335	0.5223	28.07	0.0186	8.13
Gold-coated diffuser	0.5623	0.4057	36.28	0.0112	3.47

The two samples with depolarization profiles not well fit by Gaussian curves, the screen mesh and nylon plastic material, are displayed in Fig. 11. The nylon plastic material has a very flat depolarization profile as a function of sample rotation angle, while the screen mesh exhibits an asymmetric profile. Both of these depolarization profiles are expected from the diagonal components of their MmBRDF plots (see Section 3). Volume (bulk) scattering and the multiple scattering associated with the diffusion of light in the nylon material likely account for its flat profile and near-zero Gaussian amplitude. Much of the light's interaction occurs inside the material rather than at the surface, and this bulk scattering tends to randomize the polarization of the scattered light.
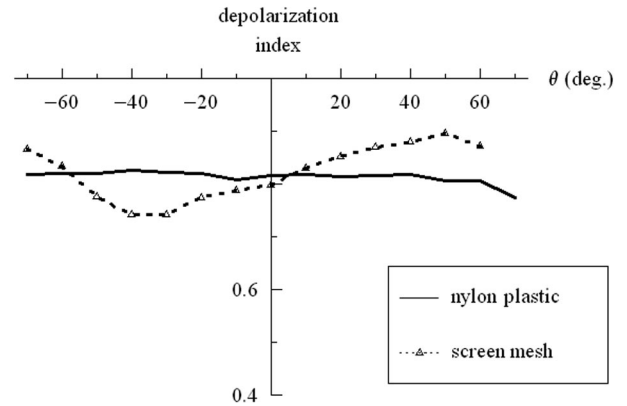

Fig. 11. Depolarization profiles as a function of sample rotation angle for the nylon plastic and screen mesh samples.
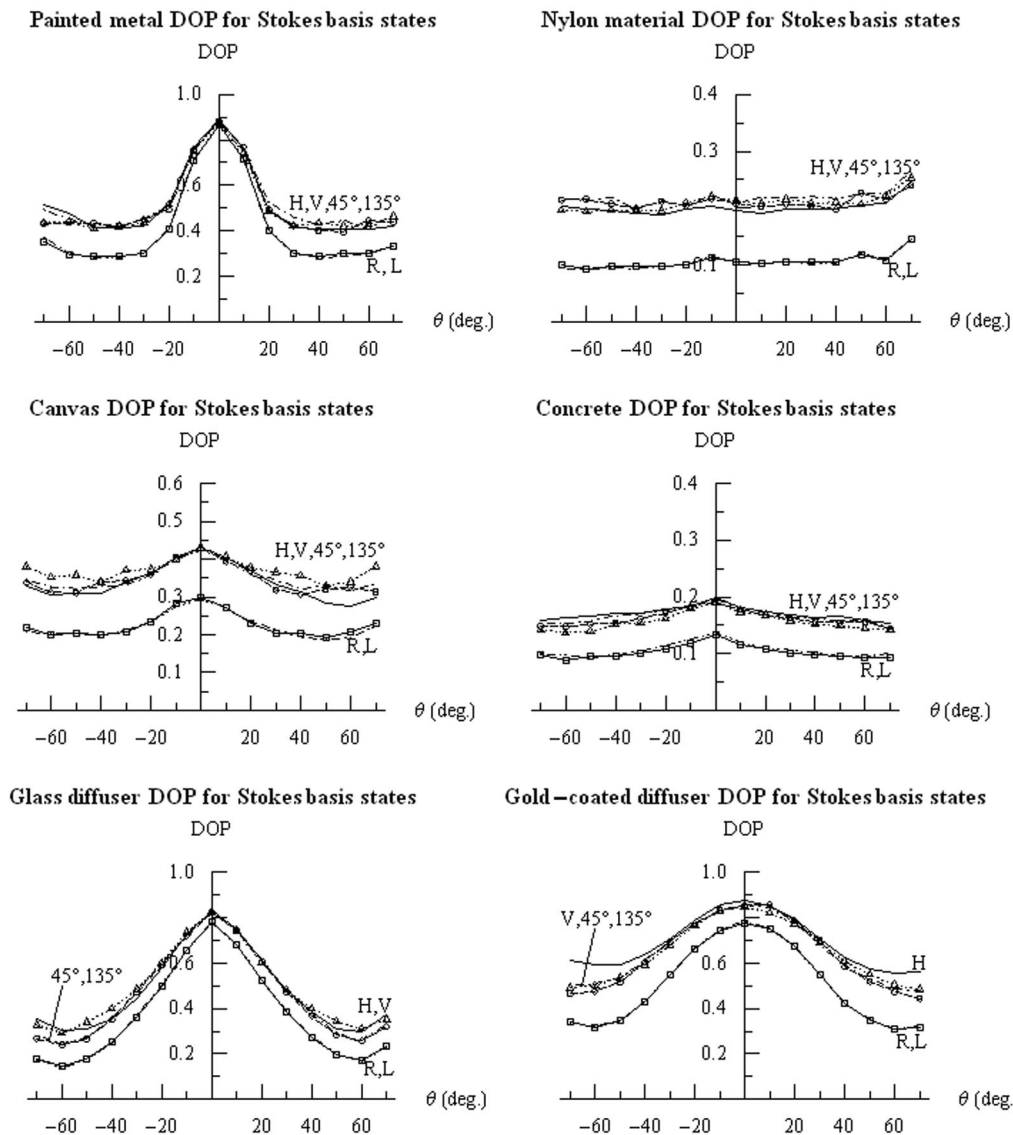

Fig. 12. DOP in response to the six Stokes basis states for six samples. Circularly polarized light is consistently depolarized more than linearly polarized light. Solid curves, H, horizontal; dotted curves with triangles, V, vertical; dotted–dashed curves, 45°; dashed curves with circles, 135°; dotted–dotted–dashed curves, R, right-circular; solid curves with squares, L, left-circular.

5. Degree of Polarization Variations with Incident State

The DOP of light scattered or diffusely reflected from samples usually varies with the incident Stokes vector. Equations (A8) and (A9) discuss the Mueller matrices for several nonuniform depolarizer types. Figure 12 plots the scattered DOP as a function of sample rotation for the six Stokes basis states: horizontal, vertical, 45°, 135°, right-circular, and left-circular polarization.

For most samples the depolarization of each linear state is nearly equal. Similarly the depolarization of both circular states is nearly equal, within 0.01. The depolarization difference between linear and circular states is significant; circular states are depolarized more than linear states. This increased depolarization of circular states is consistent with results from Lewis *et al.*, who measured a rough aluminum surface,[16] and with the scattering theory from Mishchenko and Hovenier.[13] Three of the more reflective samples, the green painted metal and the two diffuser samples, exhibit less difference between the depolarization of circular and linear states. The linear–circular depolarization difference for these samples is smallest for the specular reflection condition and increases for higher sample rotation angles. Strong depolarizers like the canvas, nylon plastic material, and concrete exhibit a nearly constant linear–circular depolarization difference with changing sample rotation angle. The DOP of circular states is typically 0.1 to 0.2 less than the DOP of linear states for greater sample rotation angles.

Depolarization of the four linear Stokes basis states is similar. For the glass diffuser a slight separation between the response to horizontal and vertical input states and the 45° and 135° input states appear at higher sample rotation angles (bottom left in Fig. 12). Other samples have small, possibly random variation between the output degrees of polarization of incident H and V basis states and incident 45° and 135° basis states. The degrees of polarization of these basis state pairs remain mostly within 6% of each other. The glass diffuser and the canvas show a slight preference for depolarizing horizontal (*p*) polarization more than vertical (*s*) polarization. For the gold-coated diffuser, horizontally polarized light depolarizes less than the vertical (*s*-polarized) light.

6. Discussion and Conclusion

MmBRDF data and depolarization measurements aid in the characterization of surfaces and materials. Combinations of Mueller elements yield the diattenuation, retardance, and depolarization properties, which might serve to discriminate between surface types.

Depolarization characteristics offer a metric for scattering surface properties such as roughness or reflectivity with large dynamic range. The depolarization index as a function of scatter angle was well fit by an inverted Gaussian profile for all the spatially homogeneous scattering samples except the nylon plastic material. The Gaussian width, amplitude, depolarization value at large sample rotation angles

(i.e., Gaussian asymptote), and steepness factor (amplitude-to-width ratio) were calculated as potential sample discriminants, and some qualitative correlations with surface roughness and reflectivity were observed. As a function of sample rotation angle, smoother samples display steep Gaussian profiles with larger amplitude-to-width ratios. The most reflective samples exhibited less depolarization.

Among the six Stokes vector basis states, circular states are depolarized more than linear states for every sample. For more reflective samples, the difference between linear and circular depolarization decreases near the specular reflection condition, whereas less reflective samples have a nearly constant difference between linear and circular depolarization. Circular depolarization clearly behaves differently from linear depolarization, and the difference as a function of sample rotation angle provides additional information regarding the sample.

This work has surveyed seven different man-made samples. Additional investigations are being prepared with a series of bistatic angles in addition to in-plane and out-of-plane MmBRDF measurements.

Exploitation of polarization scatter data for remote sensing is promising. It is evident that scatter polarization properties depend on surface and material characteristics such as refractive index, roughness, and texture. Thus the MmBRDF curves and reduced depolarization profiles offer a powerful method for investigating, comparing, and classifying targets in remote sensing.

Appendix A: Mueller Matrices, Mueller Matrix Images, and Depolarization Metrics

The 4×4 element Mueller matrix describes the transformation of arbitrary incident Stokes vectors to output Stokes vectors:

$$\begin{bmatrix} S_0' \\ S_1' \\ S_2' \\ S_3' \end{bmatrix} = \begin{bmatrix} m_{11} & m_{12} & m_{13} & m_{14} \\ m_{21} & m_{22} & m_{23} & m_{24} \\ m_{31} & m_{32} & m_{33} & m_{34} \\ m_{41} & m_{42} & m_{43} & m_{44} \end{bmatrix} \begin{bmatrix} S_0 \\ S_1 \\ S_2 \\ S_3 \end{bmatrix}. \quad (A1)$$

A Mueller matrix contains a complete polarization coupling characterization of a surface for a specified wavelength, incident solid angle, and collected solid angle. All Mueller matrices presented here are normalized by the m_{11} element (upper left component) except for the m_{11} element itself:

$$\tilde{M} = \begin{bmatrix} m_{11} & m_{12}/m_{11} & m_{13}/m_{11} & m_{14}/m_{11} \\ m_{21}/m_{11} & m_{22}/m_{11} & m_{23}/m_{11} & m_{24}/m_{11} \\ m_{31}/m_{11} & m_{32}/m_{11} & m_{33}/m_{11} & m_{34}/m_{11} \\ m_{41}/m_{11} & m_{42}/m_{11} & m_{43}/m_{11} & m_{44}/m_{11} \end{bmatrix}. \quad (A2)$$

Normalization limits all element values to the range of $-1 \leq m_{ij} \leq 1$, facilitating comparison of Mueller matrix data to Mueller matrices of polarizers and retarders tabulated in the literature or presented in functional form. The unnormalized m_{11} element for a
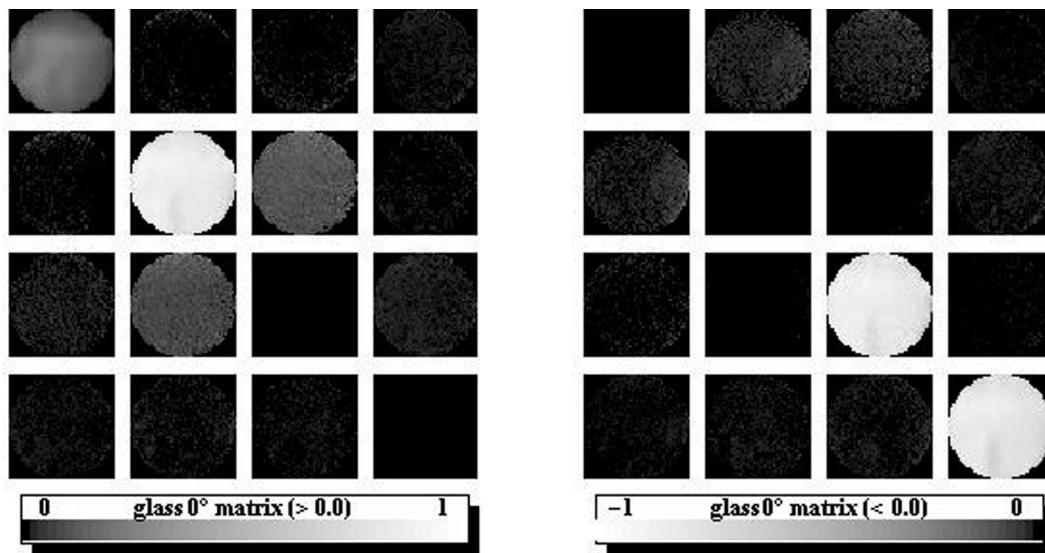
Fig. 13. Mueller matrix image of scattered light from a glass diffuser illuminated with a collimated beam. Normalized Mueller matrix images range from −1 to 1. Here the positive Mueller matrix values are displayed in the left panel and the negative values are displayed in the right panel with black indicating zero in both image arrays since gray-scale printing does not lend itself well to displaying the positive and negative values in a single image.

diffusely reflecting sample corresponds to the BRDF [defined in Eq. (B1)] for unpolarized illumination.

Mueller matrix images characterize the polarization transformations for an array of small area elements across a scene as imaged onto the pixels of a CCD camera. A Mueller matrix image is displayed as a 4×4 array of images, where each component image represents the corresponding normalized Mueller matrix element array. An example Mueller matrix image of diffusely reflected light is displayed in Fig. 13, where each Mueller component image contains 64×64 pixels of information.

A sign change in the Mueller calculus coordinate system occurs upon reflection in our notation. After reflection, the S_2 component of Stokes vectors (linearly polarized light at 45° and 135°) and the S_3 component (circularly polarized light) change sign. The S_2 component changes sign during diffuse reflection because the z component of the light propagation vector (the component parallel to the sample surface normal) changes sign. To maintain a right-handed coordinate system, one of the transverse coordinates must change sign as well. In this work, coordinates (x, y, z) switch to $(x, -y, -z)$ after diffuse reflection from the sample. The change of coordinates dictates that a beam polarized at an angle of 45° that reflects polarized in the same global plane is described as having a 135° orientation in the coordinates following reflection. In addition, the helicity (i.e., handedness) of all circular and elliptical states changes sign upon reflection. Right-circular polarization reflects as left-circular polarization, and vice versa. These sign changes apply to all matrices presented here since this study characterizes only light that has been backscattered or diffusely reflected from the sample. With this convention for reflection, the equation for rotating the Mueller matrix **M** of a sample measured

by a polarimeter in a reflection configuration is

$$
\begin{aligned}
\mathbf{M}_R(\theta) &= \mathbf{R}(\theta) \cdot \mathbf{M} \cdot \mathbf{R}(\theta) \\
&= \begin{bmatrix} 1 & 0 & 0 & 0 \\ 0 & \cos(\theta) & -\sin(\theta) & 0 \\ 0 & \sin(\theta) & \cos(\theta) & 0 \\ 0 & 0 & 0 & 1 \end{bmatrix} \begin{bmatrix} m_{11} & m_{12} & m_{13} & m_{14} \\ m_{21} & m_{22} & m_{23} & m_{24} \\ m_{31} & m_{32} & m_{33} & m_{34} \\ m_{41} & m_{42} & m_{43} & m_{44} \end{bmatrix} \\
&\times \begin{bmatrix} 1 & 0 & 0 & 0 \\ 0 & \cos(\theta) & -\sin(\theta) & 0 \\ 0 & \sin(\theta) & \cos(\theta) & 0 \\ 0 & 0 & 0 & 1 \end{bmatrix}
\end{aligned}
\tag{A3}
$$

compared with

$$
\mathbf{M}_T(\theta) = \mathbf{R}(-\theta) \cdot \mathbf{M} \cdot \mathbf{R}(\theta)
\tag{A4}
$$

for Mueller matrices in transmission. For example, the Mueller matrix of a transmission polarizer with its transmission axis oriented at 20° and the Mueller matrix of a reflection polarizer oriented at 20° are different since polarized light exits the reflection polarizer oriented at −20° in the reflection coordinates (20° in the incident coordinates). In essence the reflection polarizer is analyzing at 20° but polarizing at −20°. For the special cases of linear polarizer matrices oriented at 0° or 90° and linear retarders oriented at 0° or 90°, the Mueller matrices are the same for transmission and reflection. Equation (A3) does not strictly hold for scattering samples, which likely exhibit Mueller matrices static with respect to rotations about their normal.

The normalized reflection Mueller matrices for weakly polarizing diffuse reflecting samples, those with diattenuation, retardance, and depolarization

close to zero, are close to the Mueller matrix for an ideal reflector:

$$\mathbf{M}_{\text{refl}} = \begin{bmatrix} 1 & 0 & 0 & 0 \\ 0 & 1 & 0 & 0 \\ 0 & 0 & -1 & 0 \\ 0 & 0 & 0 & -1 \end{bmatrix}. \quad (A5)$$

$\mathbf{M}_{\text{refl}}$ is the Mueller matrix for reflection or scatter in the absence of polarization effects. For the measurements in this study, m_{11} and m_{22} are always positive and m_{33} and m_{44} are always negative.

The retardance and diattenuation properties of the Mueller matrices presented here are calculated using the polar decomposition of Lu and Chipman[21,22]:

$$\mathbf{M} = \mathbf{M}_{\text{depol}}\mathbf{M}_{\text{ret}}\mathbf{M}_{\text{diat}}. \quad (A6)$$

Depolarization properties are calculated directly from the Mueller matrix using the depolarization index [described in Eq. (A10) below]. The samples presented here show negligible retardance, a trait typical of rough scattering samples. A small amount of diattenuation is observed for some samples, and all samples exhibit significant depolarization.

Scattering samples depolarize different incident polarized states by different amounts. Several different equations to quantify depolarization effects of a Mueller matrix have been developed.[23–25] Depolarization may be understood in terms of reduction of the DOP of Stokes vectors:

$$\text{DOP}(\mathbf{S}) = \frac{\sqrt{S_1^2 + S_2^2 + S_3^2}}{S_0}. \quad (A7)$$

A partially depolarizing Mueller matrix $\mathbf{M}$ changes a completely polarized state (DOP of 1) into an exiting state $\mathbf{S}'$ with DOP less than or equal to 1. Hence, $1 - \text{DOP}(\mathbf{S}') = 1 - \text{DOP}(\mathbf{M} \cdot \mathbf{S})$ is a measure of the depolarization of incident polarized state $\mathbf{S}$ by $\mathbf{M}$.

The Mueller matrices for an ideal depolarizer (ID) and for a diffusely reflecting uniform depolarizer (UD) or diagonal nonuniform depolarizer (DNUD), respectively, are

$$\text{ID} = \begin{bmatrix} 1 & 0 & 0 & 0 \\ 0 & 0 & 0 & 0 \\ 0 & 0 & 0 & 0 \\ 0 & 0 & 0 & 0 \end{bmatrix},$$

$$\text{UD} = \begin{bmatrix} 1 & 0 & 0 & 0 \\ 0 & a & 0 & 0 \\ 0 & 0 & -a & 0 \\ 0 & 0 & 0 & -a \end{bmatrix},$$

$$\text{DNUD} = \begin{bmatrix} 1 & 0 & 0 & 0 \\ 0 & a & 0 & 0 \\ 0 & 0 & -b & 0 \\ 0 & 0 & 0 & -c \end{bmatrix}. \quad (A8)$$

ID completely depolarizes all incident states; only unpolarized light exits. UD partially depolarizes all states equally upon reflection or scatter. DNUD partially depolarizes horizontal and vertical states equally to a DOP of a, 45° and 135° states equally to a DOP of b, and right- and left-circular states to a DOP of c. For the nonuniform depolarizer (NUD) Mueller matrix,

$$\text{NUD} = \begin{bmatrix} 1 & 0 & 0 & 0 \\ m_{21} & m_{22} & 0 & 0 \\ m_{31} & 0 & m_{33} & 0 \\ m_{41} & 0 & 0 & m_{44} \end{bmatrix}, \quad (A9)$$

the horizontal and vertical states are depolarized differently, as are 45° and 135° and the right- and left-circular states. The first column contains depolarization differences between the orthogonal basis states such that horizontal light is depolarized to a DOP of $m_{22} + m_{21}$ while vertical light is depolarized to $m_{22} - m_{21}$, etc. This list of depolarizing forms is not comprehensive, and other Mueller matrix depolarizing forms occur.

Two single number metrics are defined in the literature to quantify Mueller matrix depolarization, the average DOP and the depolarization index. The average DOP is defined as the average exiting DOP calculated by integrating over all incident states $\mathbf{S}$ on the surface of the Poincaré sphere. The average DOP is computed using numerical integration routines and is therefore a computationally intensive procedure. For example, calculating the average DOP for our 64×64 pixel Mueller matrix images requires approximately 1 min.

Depolarization is quantified here by the depolarization index $\text{Dep}(\mathbf{M})$ equal to one minus the depolarization metric of Gil and Bernabeu[23,24]:

$$\text{Dep}(\mathbf{M}) = 1 - \frac{\sqrt{\left(\sum_{i,j} m_{ij}^2\right) - m_{11}^2}}{\sqrt{3}m_{11}}. \quad (A10)$$

$\text{Dep}(\mathbf{M})$ is unity for the ID and equals $1 - a$ for a UD [see Eq. (A8)]. $\text{Dep}(\mathbf{M})$ equals zero for all nondepolarizing Mueller matrices. It has been argued that average DOP is more relevant and understandable than the depolarization index.[26] However, for all the Mueller matrices of homogeneous samples measured in this work, the rms difference between these two depolarization metrics across all angles of incidence and scatter is less than 0.01. The two metrics being nearly indistinguishable for these Mueller matrix data sets, the depolarization index of Eq. (A10) was selected for presentation here on the merit of its more rapid computation.

Appendix B: Mueller Matrix Bidirectional Reflectance Distribution Function Geometry and Measurement

The conventional function for characterizing the diffuse reflection of light, the BRDF, is readily general-
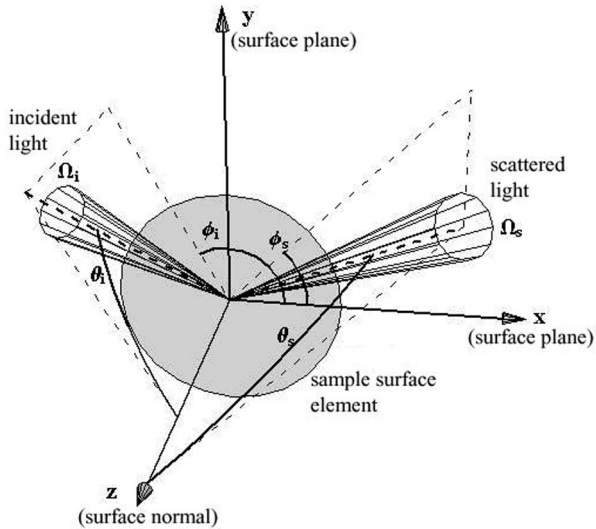
Fig. 14. Coordinate system for scattered light measurement. θ_i is the angle of incidence of a beam of solid angle Ω_i on a surface element with surface normal z. θ_s is the angle from the sample surface normal at which a solid angle Ω_s of diffusely reflected light is collected. The planes of incidence and scatter are rotated from the x–z plane of reference by angles ϕ_i and ϕ_s, respectively.

ized to incorporate polarization effects by using the MmBRDF. Light scattering from a surface or differential surface area is described by four angles in a spherical coordinate system as displayed in Fig. 14. The directions of the incident light cone (of solid angle Ω_i) and the scattered light cone (solid angle Ω_s) are described with respect to the surface normal z and an arbitrary in-plane axis x. The azimuth angle ϕ_i defines rotation of the plane of incidence from the x–z plane, and θ_i is the declination angle in the plane of incidence with respect to z. Likewise, ϕ_s and θ_s define the direction of scattered light collection with respect to the same coordinate system.

Light scattering from surfaces due to their diffuse and specular reflectance is commonly characterized by the BRDF, which describes differential output radiance from a surface normalized by differential incident irradiance as a function of the angles of incidence and scatter[3]:

$$\mathrm{BRDF}(\varphi_i, \ \theta_i, \ \varphi_s, \ \theta_s) = \frac{\mathrm{d}L_s(\varphi_s, \ \theta_s)}{\mathrm{d}E_i(\varphi_i, \ \theta_i)}. \quad \text{(B1)}$$

This standard BRDF definition makes no reference to the incident polarization state. In scatter polarization the BRDF function is generalized to arbitrary incident polarization states by replacing the scalar BRDF with Mueller matrices, yielding the MmBRDF. The MmBRDF provides the magnitudes of the Mueller matrix elements describing a sample as a function of the four-angle scatter geometry of Fig. 14:

$$\mathrm{MmBRDF}(\varphi_i, \ \theta_i, \ \varphi_s, \ \theta_s) =$$
$$\begin{bmatrix} m_{11}(\varphi_i, \ \theta_i, \ \varphi_s, \ \theta_s) & \dots & m_{14}(\varphi_i, \ \theta_i, \ \varphi_s, \ \theta_s) \\ \vdots & \ddots & \vdots \\ m_{41}(\varphi_i, \ \theta_i, \ \varphi_s, \ \theta_s) & \dots & m_{44}(\varphi_i, \ \theta_i, \ \varphi_s, \ \theta_s) \end{bmatrix}. \quad \text{(B2)}$$

The multiplicative factor converting the reflective polarization conversion efficiencies of the MmBRDF to units of inverse steradians [as in the BRDF definition of Eq. (B1)] is simply the inverse of the solid angle subtended by the collection optics as viewed by the sample. For our measurement configuration [with 1 in. (2.54 cm) collection optics 20 in. (50.8 cm) distant from the sample], this factor is 509.6 sr^{-1}. Normalization of the last 15 MmBRDF elements by the m_{11} element simplifies the interpretation of polarization properties associated with scattering by placing all values on a -1 to 1 scale.

References

1. H. C. van de Hulst, *Light Scattering by Small Particles* (Dover, 1981).
2. P. Beckman and A. Spizzichino, *Scattering of Electromagnetic Radiation from Rough Surfaces* (Franklin, 1963).
3. J. C. Stover, *Optical Scatter Measurement and Analysis*, 2nd ed. (SPIE Press, 1995).
4. J. L. Pezzaniti and R. A. Chipman, "Mueller matrix scatter polarimetry of a diamond-turned mirror," Opt. Eng. **34,** 1593–1598 (1995).
5. E. A. Sornsin and R. A. Chipman, "Polarization BRDF of satellite materials," presented at the Workshop on Infrared and Millimeter Wave Polarimetry, Redstone Arsenal, Alabama, 5–7 December 1995.
6. S.-M. F. Nee and T.-W. Nee, "Principal Mueller matrix of reflection and scattering for a one-dimensional rough surface," Opt. Eng. **41,** 994–1001 (2002).
7. K. A. O'Donnell and M. E. Knotts, "Polarization dependence of scattering from one-dimensional rough surfaces," J. Opt. Soc. Am. A **8,** 1126–1131 (1991).
8. T. R. Michael, M. E. Knotts, and K. A. O'Donnell, "Stokes Matrix of a one-dimensional perfectly conducting rough surface," J. Opt. Soc. Am. A **9,** 585–596 (1992).
9. G. Videen, J.-Y. Hsu, W. S. Bickel, and W. Wolfe, "Polarized light scattered from rough surfaces," J. Opt. Soc. Am. A **9,** 1111–1118 (1992).
10. F. Schiff, J. C. Stover, D. R. Bjork, and B. D. Swimley, "Mueller matrix measurements of scattered light," in *Polarization Analysis and Measurement*, R. Chipman and D. Goldstein, eds., Proc. SPIE **1746,** 311–318 (1992).
11. E. R. Mendez, A. G. Navarrete, and R. E. Luna, "Statistics of the polarization properties of one-dimensional randomly rough surfaces," J. Opt. Soc. Am. A **12,** 2507–2516 (1995).
12. S.-M. F. Nee and T.-W. Nee, "Polarization of scattering by rough surfaces," in *Scattering and Surface Roughness II*, Z. H. Gu and A. A. Maradudin, eds., Proc. SPIE **3426,** 169–180 (1998).

13. M. I. Mishchenko and J. W. Hovenier, "Depolarization of light backscattered by randomly oriented nonspherical particles," Opt. Lett. **20,** 1356–1358 (1995).

14. K. H. Jun, J. H. Kwak, and K. S. Lim, "Simulation of depolarization effect by a rough surface for spectroscopic ellipsometry," J. Opt. Soc. Am. A **20,** 1060–1066 (2003).

15. M. W. Williams, "Depolarization and cross polarization in ellipsometry of rough surfaces," Appl. Opt. **25,** 3616–3621 (1986).

16. G. D. Lewis, D. L. Jordan, and E. Jakeman, "Backscatter linear and circular polarization analysis of roughened aluminum," Appl. Opt. **37,** 5985–5992 (1998).

17. B. G. Hoover, D. C. Dayton, and J. E. Havey, "Active detection of off-diagonal Mueller elements of rough targets," in *Polarization Science and Remote Sensing*, J. A. Shaw and J. S. Tyo, eds., Proc. SPIE **5158,** 226–238 (2003).

18. T. A. Germer and M. E. Nadal, "Modeling the appearance of special effect pigment coatings," in *Surface Scattering and Diffraction for Advanced Metrology*, Z.-H. Gu and A. A. Maradudin, eds., Proc. SPIE **4447,** 77–86 (2001).

19. T. A. Germer and E. Marx, "Ray model of light scattering by flake pigments or rough surfaces with smooth transparent coatings," Appl. Opt. **43,** 1266–1274 (2004).

20. M. H. Smith, "Optimization of a dual-rotating-retarder Mueller matrix imaging polarimeter," Appl. Opt. **41,** 2488–2493 (2002).

21. S.-Y. Lu, "An interpretation of polarization matrices," Ph.D. dissertation (Department of Physics, University of Alabama at Huntsville, 1995).

22. S.-Y. Lu and R. A. Chipman, "Interpretation of Mueller matrices based on polar decomposition," J. Opt. Soc. Am. A **13,** 1106–1113 (1996).

23. J. J. Gil and E. Bernabeu, "A depolarization criterion in Mueller matrices," Opt. Acta **32,** 259–261 (1985).

24. J. J. Gil and E. Bernabeu, "Depolarization and polarization indices of an optical system," Opt. Acta **33,** 185–189 (1986).

25. R. A. Chipman, "Polarimetry," in *Handbook of Optics* (McGraw-Hill, 1995), Vol. 2.

26. R. A. Chipman, "Depolarization index and the average degree of polarization," Appl. Opt. **44,** 2490–2495 (2005).